Acta Astronautica 143 (2018) 105–117

Contents lists available at ScienceDirect

Acta Astronautica

journal homepage: www.elsevier.com/locate/actaastro

New technologies for ammonium dinitramide based monopropellant thrusters – The project RHEFORM

Michele Negri [a,*], Marius Wilhelm [a], Christian Hendrich [a], Niklas Wingborg [b], Linus Gediminas [b], Leif Adelöw [b], Corentin Maleix [c], Pierre Chabernaud [c], Rachid Brahmi [c], Romain Beauchet [c], Yann Batonneau [c], Charles Kappenstein [c], Robert-Jan Koopmans [d], Sebastian Schuh [d], Tobias Bartok [d], Carsten Scharlemann [e], Ulrich Gotzig [f], Martin Schwentenwein [g]

[a] *DLR, German Aerospace Center, Institute of Space Propulsion, Lampoldshausen, Langer Grund, 74239 Hardthausen, Germany*
[b] *FOI, Swedish Defence Research Agency, SE-14725 Tumba, Sweden*
[c] *IC2MP, CNRS-UMR 7285, University of Poitiers, 4 rue Michel Brunet, bâtiment B27, TSA 51106, 86073 Poitiers Cedex 9, France*
[d] *FOTEC Forschungs- und Technologietransfer GmbH, Viktor Kaplan-Straße 2, 2700 Wiener Neustadt, Austria*
[e] *Fachhochschule Wiener Neustadt, Johannes Gutenberg-Straße 3, 2700 Wiener Neustadt, Austria*
[f] *Ariane Group, Langer Grund, 74239 Hardthausen, Germany*
[g] *Lithoz GmbH, Mollardgasse 85a/2/64-69, 1060 Vienna, Austria*

ARTICLE INFO

Keywords:
Green propellant
Ammonium dinitramide (ADN)
Hydrazine replacement
Catalyst development
Catalytic ignition
Thermal ignition

ABSTRACT

New technologies are developed in the project RHEFORM to enable the replacement of hydrazine with liquid propellants based on ammonium dinitramide (ADN). The replacement of hydrazine with green propellants will make space propulsion more sustainable and better suitable for the requirements of future missions. In the RHEFORM project investigation on the composition of the propellants are conducted to enable the use of materials for catalysts and combustion chambers which are not subject to the International Traffic in Arms Regulations (ITAR). New igniters are under development aiming at a reduction of required energy and a more prompt ignition. Two different types of igniters are considered: improved catalytic igniters and thermal igniters. The technologies developed in RHEFORM will be implemented in two thruster demonstrators, aiming at a technology readiness level (TRL) of 5. In the present work the results obtained in the first half of the project are presented.

1. Introduction

The goal of the EU Horizon2020 project RHEFORM is to develop technological solutions to overcome some of the limitations of the recently developed ionic liquids in general and ADN monopropellant blends in particular. RHEFORM started in 2015 and will run until the end of 2017 [1].

Monopropellant systems are used when simplicity, reliability and low cost are priorities and the required total impulse is low (in Ref. [2] is shown that monopropellant systems are lighter than bipropellants when the total impulse is smaller than 45 000 N-s). The proposed paper is focused on monopropellants; therefore green bipropellants are considered beyond the scope of the paper. The standard monopropellant for spacecraft since the 1960s is hydrazine. Therefore, propulsion systems based on hydrazine have large heritage. However, this propellant is highly toxic and carcinogenic, increasing the complexity and cost of testing, shipping, handling and launch preparation. In 2011 hydrazine was added to the candidate list of substances of very high concern (SVHC) by European Union under the Registration Evaluation Authorisation and Restriction of Chemicals (REACH) law [3]. Both NASA and ESA are looking for alternatives to hydrazine to be commercially available in the near to mid-term. The substitution of hydrazine with green propellants may lead to significant benefits, if suitable propellants are selected. Very interesting replacements for hydrazine are liquid propellants based on ammonium dinitramide (ADN, $NH_4^+ N(NO_2)_2^-$). They offer the following advantages compared to hydrazine:

- Simplified handling, especially loading at the launch site. During the PRISMA mission the man-hours for loading hydrazine were three times more than for LMP-103S [4].
- Higher overall performance (I_{sp}), as was shown by the PRISMA mission [5].

---

* Corresponding author.
E-mail address: michele.negri@dlr.de (M. Negri).

https://doi.org/10.1016/j.actaastro.2017.11.016
Received 11 July 2017; Received in revised form 13 November 2017; Accepted 17 November 2017

- Higher volumetric specific impulse due to higher density leading to smaller tanks, and therefore reduced structural weight [5].

ADN-based monopropellants have these major advantages, but also some limitations. The combustion temperature of LMP-103S, the most mature propellant blend, is 1630 °C. Thus it is much higher than the one of hydrazine, which is about 900 °C depending on the amount of ammonia dissociation [6]. In order to withstand these temperatures, combustion chambers from materials that are ITAR regulated are currently used. Cheaper and ITAR-free combustion chamber materials could be used, if the combustion temperature of the propellants is reduced. A second disadvantage is that the catalyst used to decompose and ignite the propellant blend requires pre-heating. The catalyst is currently electrically pre-heated to a temperature of about 350 °C, which takes around 30 min before firing, to ensure decomposition of the propellant followed by sustained and complete combustion. Objective of the project is the development of ignition systems that require less pre-heating energy. For this purpose, the possibility of improving the catalyst is researched and the use of thermal ignition is investigated. The results will be tested in a thruster demonstrator by the end of the project, aiming at a Technology Readiness Level (TRL) of 5.

2. Overview of the RHEFORM project

The project consortium of RHEFORM combines European competences in various fields, thus increasing the chances of developing innovative technologies. Two universities are involved: the University of Poitiers (UP), working mainly on catalyst chemistry and the University of Applied Sciences Wiener Neustadt (FHWN), focusing on catalysts design and testing. Three large research institutions are involved: the German Aerospace Centre (DLR) focusing on thermal ignition and thruster testing, the Swedish Defence Research Agency (FOI) with focuses on propellants development and improving the production method of ADN, and the French National Centre for Scientific Research (CNRS) working on catalyst development. Two small companies are involved: Lithoz, developing 3D printed catalyst supports and FOTEC, designing and modelling the catalyst. Finally two space companies are involved, ECAPS, the first company to demonstrate an ADN thruster in space, working in the project on the development and testing of two thruster demonstrator units, and ArianeGroup (AG) which defines the system requirements and will develop a commercialization plan from the results of RHEFORM.

A flow chart of the RHEFORM project is given in Fig. 1. The activities indicated in green have been concluded, the ones in yellow are taking place as this article has been written and the ones in white have not started yet. The present work describes the results obtained in the first half of the project, up to the development of the ignition systems. In particular Section 3 describes the rationale behind the selection of two reference cases and how the corresponding system requirements have been defined. Different variations on two existing propellants have been investigated, as detailed in Section 4. The development of catalysts is described in Section 5. Section 6 covers the research conducted on thermal ignition.

3. Definition of requirements

Two thrust classes have been selected in the project RHEFORM as references, based on a market analysis. The most urgent need of green thrusters was identified in the 20 N and in the 200 N classes. These classes have the highest market volume, after the 1 N thrusters, which are already commercialized by ECAPS. 20 N hydrazine thrusters are more common than 10 N ones. For larger thrusters a thrust level of 200 N is more common than one of 400 N. Above 400 N the need for orbital thrusters is small.

For each of the two thrust classes a reference case has been identified. The Planck scientific satellite, a space observatory operated by ESA, has been selected as a typical application for the 20 N thrusters. This satellite has an Attitude and Orbit Control Systems (AOCS) which uses hydrazine as monopropellant. The AOCS is equipped with twelve 20 N thrusters, arranged in two redundant and independently operable branches of six thrusters each, and with four 1 N thrusters, arranged in the same independent branches with two units in each branch [7]. Based on this reference case the performance requirements for the 20 N thruster have been defined and are summarized in Table 1.

The Roll and Attitude Control System (RACS) of the VEGA launcher has been taken as a reference case for the 200 N thruster [8]. This hydrazine RACS is mounted to the AVUM (Attitude Vernier Upper Module) 4th stage and is designed to fulfil the following functions:

1. Roll control of the launcher
2. 3-axis and spin-up orbital flight control of the AVUM 4th stage, for:
    - Attitude control during coasting and in-orbit phases.
    - Satellite pointing.
    - Satellite release manoeuvres.
    - Empty stage orientation preparatory to deorbitation.

Based on the VEGA RACS the performance requirements for the 200 N thruster have been defined and are summarized in Table 1.

4. Adaptation of propellant composition

LMP-103S and FLP-106 are used as baseline propellants for the RHEFORM project. Calculations with the NASA-CEA code [9] were conducted [10]. The influence of increased water contents in the two baseline propellants on the combustion temperatures and on the performance was studied. In Table 2 the maximum admissible combustion temperatures for several typical chamber materials are provided, based on the experience of the project partner ASL. The amounts of water to be added to LMP-103S and FLP-106, to stay within the working temperature range of the material are indicated, as well as the adiabatic combustion temperatures and the corresponding specific impulses.

The influence of the relative amount of constituents on the combustion temperature and the specific impulse was also studied. Fig. 2 presents the results for variations on the LMP-103S propellant. The x-axis shows the relative amount of ADN and the y-axis the relative amount of methanol. The amount of NH_3 (25 wt.-% in water) follows from the

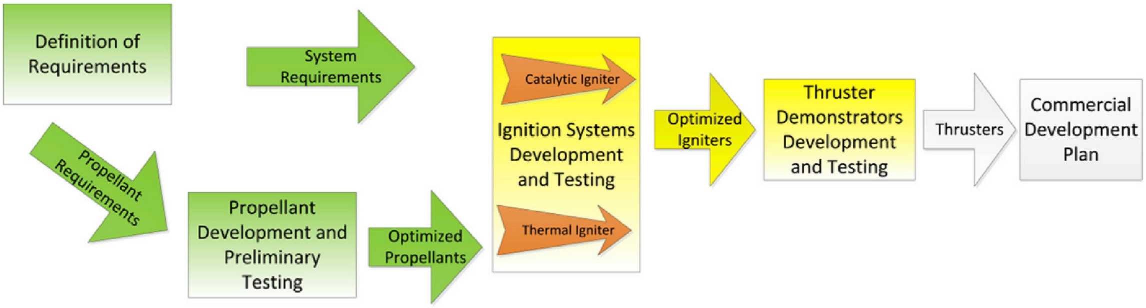

Fig. 1. Flowchart of the RHEFORM project.

Table 1
Thrusters performance requirements. BOL: Beginning of Life; EOL: End of Life; SSF: steady state firing; MIB: minimum impulse bit.

		20 N thruster AOCS			200 N thruster RACS and deorbiting		
		Minimum	Nominal	Maximum	Minimum	Nominal	Maximum
Isp in SSF	BOL		235 s			235 s	
	EOL		200 s			200 s	
MIB	BOL	0.3 N s		0.7 N s	3.2 N s		25 N s
Total Impulse					67.5 kN s		165 kN s
Steady state firing time			3600 s	5400 s	240 s	1200 s	5500 s
Number of pulses		30000			1500	8000	

Table 2
Combustion chambers materials, admissible temperatures and corresponding performances.

Combustion Chamber Material	Max admissible temperature [°C]	Propellant composition	Calculated combustion temperature [°C]	Calculated specific impulse [s]
Super Alloy	1250	LMP-103S + 17.4% H_2O	1253	226
		FLP-106 + 27.7% H_2O	1249	217
Platinum Rhodium	1500	LMP-103S + 5.8% H_2O	1499	244
		FLP-106 + 15.7% H_2O	1500	234
Platinum Iridium	1600	LMP-103S + 1.8% H_2O	1598	251
		FLP-106 + 11.5% H_2O	1601	241

The specific impulse has been calculated assuming p_c = 10 bar, ε = 40, expansion in vacuum and frozen at throat.

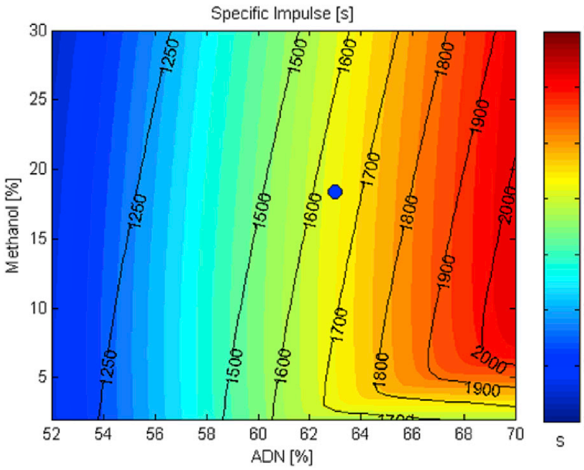

Fig. 2. Specific impulse, indicated by colours, and combustion temperature, indicated by isotherms in °C for variations in relative amount of components of LMP-103S. (For interpretation of the references to colour in this figure legend, the reader is referred to the web version of this article.)

difference between 100% and the sum of methanol and ADN weight percentages. The mass composition corresponding to the blend LMP-103S (63% ADN; 18.4% CH_3OH; 4.65% NH_3; 13.95% H_2O) is indicated with a blue dot.

In Fig. 3 the same information is shown as in Fig. 3, but now for variations of FLP-106. Here, instead of methanol, monomethylformamide (MMF) is shown on the y-axis. The remaining percentage is formed by water. The mass composition of FLP-106 (64.6% ADN; 23.9% H_2O, 11.5% MMF) is indicated with a dot.

Many research groups are working at the thermophysical and thermochemical characterization of ADN-based propellants. The density, viscosity, vapour pressure, speed of sound, and specific heat capacity of the propellant LMP-103S have been characterized by ECAPS. The results have not been published.

Thermophysical properties including saturation temperature at 0 °C, heat capacity, dynamic viscosity, thermal expansion coefficient of FLP-106 can be found in Ref. [11], those of its surface tension and vapour pressure at 25 °C can be found in Ref. [12]. Vapour pressure of both LMP-103S and FLP-106 were measured at 25 °C: 77.4 mbar (58 mmHg) for LMP-103S, and 18.7 mbar (14 mmHg) for FLP-106. Wingborg et al. [13] measured the density, specific heat capacity and electrical conductivity as function of temperature for FLP-106.

In the present work the focus of the physical and chemical analysis is on studying the influence of an increase in water content on the properties of the baseline propellants.

The propellant variations listed in Table 2 were prepared and chemically characterized using vibrational spectroscopic techniques, namely Fourier Transformed Infrared (FTIR) and laser Raman scattering spectroscopy. Of particular interest of the current work was the presence of any interaction between the components of the two baseline propellants. The influence of increasing the water content in the two baseline propellants was also investigated. The addition of water did not lead to new interactions for both FLP-106 and LMP-103S as deduced from the comparison of FTIR spectra of individual components to the spectra of the propellant and of their respective, diluted variations. It could be checked that ultrapure water contribution to the spectra increased with increasing water content of the variations analyzed, in particular for the asymmetric stretching of O—H bond centred on 3368 cm^{-1} for pure

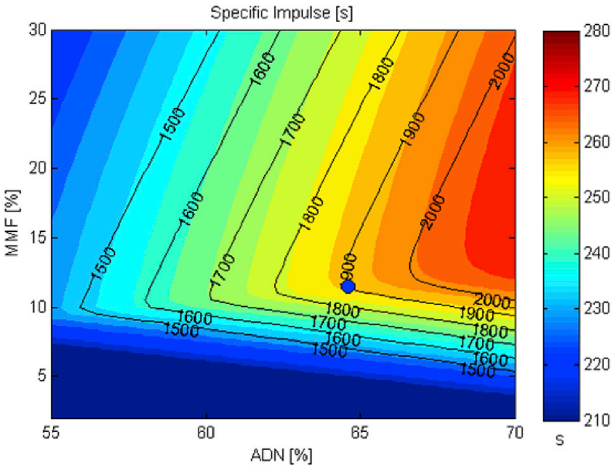

Fig. 3. Specific impulse, indicated by colours, and combustion temperature, indicated by isotherms in °C for variations in relative amount of components of FLP-106. (For interpretation of the references to colour in this figure legend, the reader is referred to the web version of this article.)

water. No particular impurities were detected either within the detection limit available from both techniques. This is relevant because ADN often contains traces of FOX-12 left over from the production process.

Strong luminescence phenomena were observed during the characterization using Raman spectroscopy with both green (514.5 nm) and red (632.8 nm) exciting laser radiations. Such phenomena were actually observed on ADN after dissolution in water, whereas other individual components, namely ammonia, ultrapure water, solid ADN, MMF and methanol did not lead to experience such problem. As a consequence, none of the mixtures containing ADN, including LMP-103S and FLP-106, could give Raman spectra without any luminescence. A more detailed analysis of vibrational transitions were hindered by the luminescent background, in particular for weaker signals. It is thus recommended to use an exciting laser source having wavelength no shorter than 785 nm, even up to 1064 nm when conducting Raman spectroscopy of mixtures containing ADN.

Propellant sampling to record a FTIR spectrum had to be optimised. Indeed, getting mid infrared spectrum in transmission mode was impossible even with a liquid film pathlength down to less than 50 μm. The mid infrared light absorption behaviour of the propellants was such that the sole use of an evanescent wave could permit to get a Fourier Transformed Infrared FTIR spectrum properly. This is of importance for efficient propellant sampling before implementing quality control on propellants using FTIR spectroscopy.

The solubility of ADN in different solvents at two temperatures (−5 and −10 °C) was also studied. In the first study, Ultraviolet–visible (UV-VIS) spectroscopy and High Performance Liquid Chromatography with Ultraviolet detection (HPLC-UV) were both used in the analysis. This study produced inhomogeneous solutions, but it could be used to see that the relative standard deviation between the three different samples (triplicates) from each tube was smaller with the former technique. Thus, only UV-VIS spectroscopy was used in the second study.

The results of the second study are shown in Table 3. The influence of different solvents on the solubility was tested using solutions of water and three organic solvents, namely monomethylformamide (like in FLP-106), formamide and dimethylformamide. As shown in the table, the relative standard deviation between the triplicates was below 1% in all cases. There seems to be little influence of the fraction of organic solvent in the ranges studied, but the trends are the expected ones, with lower solubility of ADN in the solutions with the higher fraction of organic solvent, in all cases but one. The reason for this is not known. All samples display the expected trend with lower solubility at the lower temperature.

Table 3
Results from the solubility study (FA = formamide, MMF = *N*-methylformamide, DMF = *N,N*-dimethylformamide).

Temp. [°C]	Solvent	Ratio solvent:water [w:w]	Weight fraction ADN [g/g]	Relative standard deviation [%]	Comment
−5	H_2O	–	0.606	0.8	
−5	FA:H_2O	40:60	0.611	0.2	
−5	FA:H_2O	50:50	0.600	1.1	
−5	FA:H_2O	60:40	0.606	0.1	
−5	MMF:H_2O	10:90	0.614	0.1	One outlier
−5	MMF:H_2O	20:80	0.598	0.9	
−5	MMF:H_2O	30:70	0.589	0.6	
−5	DMF:H_2O	10:90	0.612	0.7	
−5	DMF:H_2O	20:80	0.592	0.5	
−5	DMF:H_2O	30:70	0.582	0.3	
−10	H_2O	–	0.589	0.9	
−10	FA:H_2O	40:60	0.598	0.1	
−10	FA:H_2O	50:50	0.592	0.9	
−10	FA:H_2O	60:40	0.590	0.5	
−10	MMF:H_2O	10:90	0.583	0.5	
−10	MMF:H_2O	20:80	0.574	0.5	
−10	MMF:H_2O	30:70	0.554	0.9	
−10	DMF:H_2O	10:90	0.587	0.1	
−10	DMF:H_2O	20:80	0.568	0.3	
−10	DMF:H_2O	30:70	0.556	0.5	

The solubility measurements conducted are significant to develop new high-performance ADN-based propellants. In order to optimize the performances, the amount of ADN should be maximized. On the other hand, the amount of ADN should be below the solubility limit, to avoid the crystallization of ADN in the feeding line and injector. Since the solubility is strongly temperature-dependent, it is important to investigate the solubility in the complete range of operational temperatures.

5. Development of catalysts

In the RHEFORM project two types of catalyst supports are investigated: granulates and monoliths. The term "granulates" gathers different types of catalyst support shapes: grains, beads, spheres, pellets, extrudates, down to powder. Granulated catalysts are currently widely used in orbital thrusters, for example in hydrazine thrusters [14]. Monolithic catalysts are typically used in the automotive industry [15]. Also for space propulsion applications they are interesting due to reduced pressure losses, better structural stability and more accurate control of the active surface area compared to granulated beds.

5.1. Granulated catalyst development

5.1.1. Structure of granulated supports

A particular feature of granulated beds is that the presence of the chamber wall causes an ordering effect of the particles in the vicinity of the wall [16]. The degree of ordering, as well as the extent of the bed that is affected by it, is dependent on the particle geometry (spherical, cylindrical, irregular shaped, etc.), the bed-to-particle diameter ratio, the particle aspect ratio and the degree of packing. Bey and Eigenberger [17] devised a model with which the average void fraction as well as the void fraction as a function of the bed radius for spherical and cylindrical pellets can be approximated. This model was used to bound the size of the granulates. For this particular study the original model was non-dimensionalised and is presented hereafter.

The model assumes that the catalyst bed can be divided into two radial regions, demarcated by a non-dimensional radial coordinate $r^{'}$ defined as

$$r^{'} = \frac{\tilde{D}(1-\tilde{r})}{2r_{min}} - 1 \tag{1}$$

here, $\tilde{D}$ is the bed-to-pellet diameter ratio, $\tilde{r}$ the non-dimensional radial position, ranging from 0 at the centre to 1 at the wall, and r_{min} a constant defined as

$$r_{min} = 0.5\left(\tilde{D} - \sqrt{\tilde{D}(\tilde{D}-2)}\right) \tag{2}$$

The local void fraction $\varepsilon_{f,loc}$ for the wall region, i.e. for $r^{'} < 0$, can be approximated by

$$\varepsilon_{f,loc} = \varepsilon_{min} + (1-\varepsilon_{min})r^{'2} \tag{3}$$

and for the core region, i.e. for $r^{'} \geq 0$, it can be approximated by

$$\varepsilon_{f,loc} = \varepsilon_0(\varepsilon_{min} - \varepsilon_0)\exp\left(-\frac{r^{'}}{c}\right)\cos\left(\frac{\pi}{b}r^{'}\right) \tag{4}$$

here ε_{min}, ε_0, b and c are constants and dependent on the shape and dimensions of the pellet. Bey and Eigenberger investigated different shapes and sizes of pellets and derived the constants from that. There are given in Table 4.

The mean void fraction $\overline{\varepsilon_f}$ is approximated by

$$\overline{\varepsilon_f} = 0.375 + 0.34\frac{1}{\tilde{D}} \tag{5}$$

For cylindrical pellet a similar model was devised by Bey and Eigenberger. The non-dimensional radial coordinate $r^{'}$ is very similar to Eq. (1) and given by

$$r^{'} = a_0\frac{\tilde{D}(1-\tilde{r})}{2r_{min}} - 1 \tag{6}$$

a_0 is an empirical factor defined by

$$a_0 = 1.8 - \frac{2}{\tilde{D}} \tag{7}$$

For the core region of the catalyst bed, i.e. $r^{'} \geq 0$, the local void fraction is equivalent to Eq. (4). The local void fraction for the wall region was determined to be

$$\varepsilon_{f,loc} = \varepsilon_{min} + (1-\varepsilon_{min})r^{'4} \tag{8}$$

For cylindrical pellets the mean void fraction can be approximated by

$$\overline{\varepsilon_f} = 0.36 + 0.1\frac{D_{ps}}{D_b} + 0.7\left(\frac{D_{ps}}{D_b}\right)^2 \tag{9}$$

here, D_{ps} is the diameter of a sphere with an equivalent volume to the cylindrical pellet under consideration. Eq. (9) was verified for $\frac{D_{ps}}{D_b} \leq 0.6$.

With the model presented above the local void fraction $\varepsilon_{f,loc}$ was computed as a function of the bed-to-pellet diameter ratio $\tilde{D}$ and the non-dimensional radial position in the catalyst bed $\tilde{r}$. The result is shown as a heat plot in Figs. 4 and 5 for spherical and cylindrical pellets, respectively. In both cases the local void fraction is unity at the (inner) wall of the bed. Both plots show that it oscillates with radius as well as $\tilde{D}$. This is a result of the ordering effect by the wall [16]. The oscillations have a higher frequency for larger $\tilde{D}$ and tend to dampen towards the centre of the catalyst bed. The void fraction oscillation damping is stronger for cylindrical particles. In fact, for cylindrical particles and large enough $\tilde{D}$ hardly any oscillations are visible anymore in the centre region. This is in contrast with spherical particles which experience even for small spheres relative to the bed diameter the influence of the wall.

The difference in oscillation behaviour can be explained by the additional degree of freedom for cylindrical pellets: apart from the diameter also the orientation of the cylinder is a variable. This behaviour was shown numerically as well as experimentally [16]. For large values of $\tilde{D}$, say $\tilde{D} \geq 8$, the region with large void fractions close to wall, i.e. $\varepsilon_f > 0.7$, is about the same in size. For smaller values of $\tilde{D}$, this region is rapidly increasing.

The pressure drop over a particulate bed is, amongst others, dependent on the (local) void fraction. Although many different pressure drop relations are described in literature, most of them are of the form [18].

$$\frac{\Delta P}{L} = K\mu u_0 + \eta\rho u_0^2 \tag{10}$$

Table 4
Constants for investigated pellets by Bey and Eigenberger [3].

shape	D_p [mm]	L_p [mm]	ε_{min}	ε_0	b	c
sphere	4.5 ± 2.0	–	0.27	0.39	0.876	10
	6.3 ± 1.0	–	0.24	0.39		
	7.5 ± 1.0	–	0.24	0.395		
	9.8 ± 1.0	–	0.24	0.41		
	14 ± 1.5	–	0.24	0.41		
cylinder	4.5	4.5	0.275	0.365	0.876	2
	6	6	0.275	0.375		
	12	12	0.3	0.42		
	6	5–20	0.275	0.365		

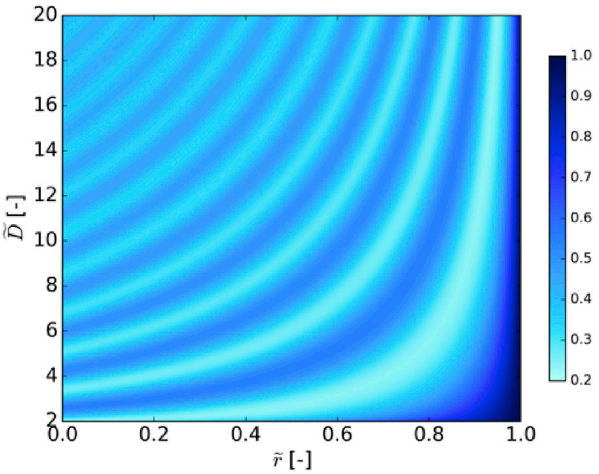

Fig. 4. Radial void fraction distribution for spherical particles.

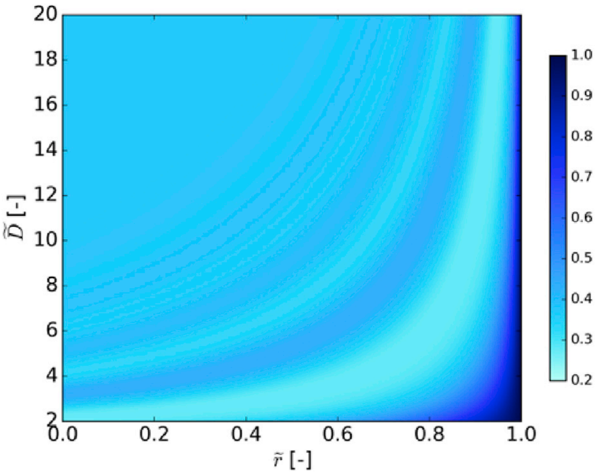

Fig. 5. Radial void fraction distribution for cylindrical particles.

here, $\Delta P/L$ is the pressure drop over the bed per unit of length, μ the dynamic viscosity, ρ the density and u_0 the superficial velocity of the fluid. K and η are factors dependent on the particle diameter and the void fraction. Many different relations were proposed in the past for K and η, of which the most famous one is the Ergun relations given by

$$K = \frac{150}{D_p^2}\frac{(1-\varepsilon_f)^2}{\varepsilon_f^3} \tag{11}$$

$$\eta = \frac{7}{4D_p}\frac{1-\varepsilon_f}{\varepsilon_f^3} \tag{12}$$

where D_p is the particle diameter. From Eqs. (10)–(12) it is clear that any variation in (local) void fraction results in a change in pressure drop. When the local void fraction changes significantly with radius, such as for low $\tilde{D}$ for spherical pellets, the corresponding variation in local pressure drop results in the formation of preferential flow paths in the bed. This effect will be more pronounced for spherical particles than for cylindrical particles when comparing Fig. 4 with Fig. 5. For this reason, this initial choice of particle shape is cylindrical. To avoid preferential flow path as much as possible, the minimum diameter ratio should be at least 8.

For higher particle diameter ratios the variation of local void fraction in radial direction will decrease. However, the total pressure drop over the bed will increase. Inspection of Eq. (10)–(12) shows that this can partly be explained by the particles diameter and partly by the void fraction, which in itself is a function of the particle diameter. Fig. 6 shows the mean void fraction as a function of the diameter ratio. Above a diameter ratio of 7–8 the change in mean void fraction is only marginal and the pressure drop will mainly depend on the particle diameter.

From the analysis above it becomes clear that a designer must always make a compromise between the reduction of preferential flow paths and reduction in pressure drop. The limited amount of design degrees of freedom generally does not allow for other considerations, such as optimising the heat transfer in the bed, to be taken into account. Note that the analysis presented above is based on average values over the length of the catalyst bed. The actual flow pattern in such beds is virtually impossible to predict a priori. In fact, for an important part it is dependent on the quality of filling [19]. Also attrition due to abrasion, caused by a certain freedom of movement of the pellets, is a problem requiring careful attention [14].

5.1.2. *Granulated supports materials*

Granulated support material should have an excellent resistance to thermal shocks and extreme temperatures, while keeping a high specific surface area. Based on these requirements, different materials have been considered: (i) gamma alumina (γ-Al_2O_3) extrudates procured from Alfa Aesar; (ii) yttria stabilized zirconia (YSZ) extrudates acquired from St Gobain NORPRO; and non-commercially available (iii) silicon-doped alumina material; and (iv) hexaaluminates. Silicon-doped alumina was synthesized to tentatively retard the gamma (with high specific surface area) to alpha alumina phase transition in the harsh working conditions. It is denoted DUS1. Hexaaluminates are hexagonal alumina phases containing a large-radius cation. Two types of structure were synthetized, namely hexaaluminate A ($LaAl_{11}O_{18}$) and hexaaluminate B ($BaAl_{12}O_{19}$).

The crystalline structure of the synthetized materials were assessed using X-ray diffraction (XRD, not shown), to get information on the nature of the crystalline phases. The granulates were also analyzed using nitrogen sorptiometry to get textural information about the carriers and the catalysts: specific surface area, pore volume and pore size. The analysis was conducted after heat treatment in air at different temperatures, in order to simulate the effect of combustion chamber conditions on the catalysts. The results are shown in Table 5.

After the heat treatment, YSZ material suffered a dramatic shrinkage and the specific surface area was decreased to a very small value. Therefore YSZ was discarded as support material. Similarly the specific surface area of the hexaaluminate A after the thermal treatment was considered too low.

5.1.3. *Granulated catalysts: active phase*

Numerous active phases were tested. The deposition of the active phase is carried out by impregnating the granules with a solution of the active phase precursor at room temperature. The solvent is then removed by gentle evaporation at moderate temperature. Catalysts are obtained subsequently to an appropriate heat treatment of the solid thus obtained. The search for the optimal nature and percentage of active phases is still ongoing, and more details will be published in a future work.

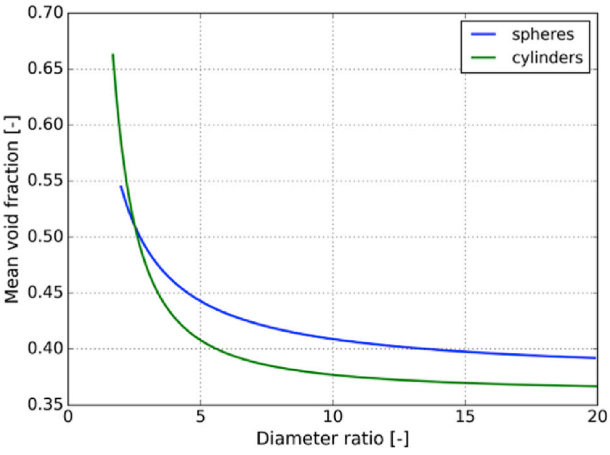

Fig. 6. Average void fraction for spherical and cylindrical particles.

Table 5
Specific surface area (a), pore volume (v_t), pore size ($Ø$) of selected support materials after heat treatment in air at different temperatures.

Materials, Shape	Thermal treatment	Specific surface area m^2/g	Pore volume cm^3/g	Pore size Å
DUS 1, Powder	(1200 °C–4 h)	92	0.247	82
Hexaaluminate A, Powder	(1500 °C–4 h)	7	0.018	118
Hexaaluminate B, Powder	(1500 °C–4 h)	46	0.063	64
YSZ, Pellets	(1500 °C–4 h)	<0.1	–	–

5.2. *Monolithic catalysts development*

5.2.1. *3D printing method*

An alternative to pellets, addressing at least part of the problems identified above, is to use of monoliths. These types of catalyst consist of one piece, avoiding the problem of attrition and no filling of the catalyst chamber required, with a priori well-defined flow paths. However, in the past the design of monoliths was restricted to straight channels. The usual manufacturing method is extrusion of a ceramic paste through a die. This limits the design freedom of the inner structure of the monolith to two dimensions only. Recently, a new technology was introduced opening up the possibilities to control the design of a catalytic bed to a much larger extent. This technology relies on additive layered manufacturing of ceramics. With this technology monolithic catalyst supports are produced using a 3D printing method called Lithography-based Ceramic Manufacturing (LCM) developed by Lithoz [20]. This methodology shapes the ceramic in form of a suspension using a photocurable ceramic suspension. In presence of an adequate photo-initiator these compounds are crosslinked upon selective exposure to light to give the green parts the necessary mechanical strength for further processing. This approach eliminates the handling of fine powders which facilitates the process in terms of safety precautions and also allows a better compaction of the ceramic powder to yield higher green densities and subsequently higher densities in the final sintered state.

The CeraFab system produces 3D parts starting from a CAD file and converts it directly into the physical object. This is accomplished in a layer-by-layer manner; the CAD file is virtually sliced into a large number of very thin layers and the single slices are cured sequentially. Fig. 7 shows the schematic working principle of the CeraFab system. The assembly comprises a rotating vat filled with the photocurable ceramic suspension. The light source irradiates the bottom side of the vat via a digital micro-mirror device. The building platform is above the vat and moves upwards the z-axis during the fabrication process.

After the structuring on the CeraFab system the green parts have to be cleaned from the excess slurry by immersing the part in an appropriate solvent capable of dissolving the slurry without damaging the cured structure. Subsequent processing involves the debinding step where the organic matrix is removed by treating the parts at elevated temperatures. The hereby obtained parts are then sintered in a high-temperature furnace to give the ceramic bodies.

5.2.2. *3D printing: manufacturing limitations*

As a first step it was investigated what the manufacturing limitations are. For this purpose three monoliths were printed from MgO. Sample 1 consisted of holes with 4 different diameters: 0.5, 0.75, 1.0 and 1.25 mm. Sample 2 and 3 consist both of equilateral triangular shaped channels with a wall thickness of 0.22 mm. A schematic of the two different structures is shown in Fig. 8.

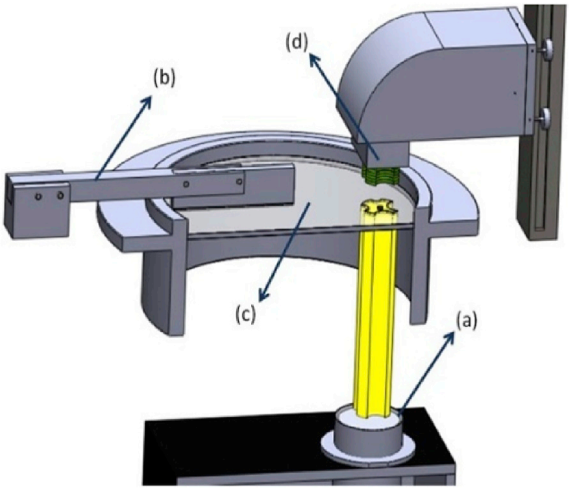

Fig. 7. Schematic principle of the LCM process: (a) Light source, (b) Coating knife, (c) Vat filled with resin and (d) Building platform, based on [21].

All cylinders had a length of 10 mm. To investigate the 3-D capabilities of the manufacturing procedure, the cylinder was twisted, i.e. the top plane was rotated relative to the bottom plane. Sample 1 and 3 were rotated 360° and sample 2 by 180°. The samples were investigated by grinding them, taking pictures of the cross section and compare the different cross section pictures with each other.

The results for sample 1 are shown in Figs. 9 and 10. Both plots show the cross sectional areas of the holes relative to the top plane as a function of the pitch. Here the pitch is defined as

$$pitch = \frac{2\pi r^2}{L} \tag{13}$$

here r is the distance of the centre of the hole to the centre of the monolith and L the required length of the monolith to rotate 360° once. The relative cross sectional areas at 4.43 and 9 mm from the top plane are shown in Figs. 9 and 10, respectively. Except for the holes with a diameter of 1.25 mm, no particular trend is discernible. One possible explanation for this is the way in which the green bodies are cleaned from the excess slurry. By immersing the green bodies in a solvent, removing excess slurry fully relies on diffusion. The smaller the hole diameter the higher the diffusion resistance and thus the lower the effective diffusion. The plots suggest that the critical diameter is between 1.0 and 1.25 mm. For holes with a diameter of 1.25 mm the pitch, or tortuosity, seems to play a role as well and become noticeable for a pitch of 2 and larger.

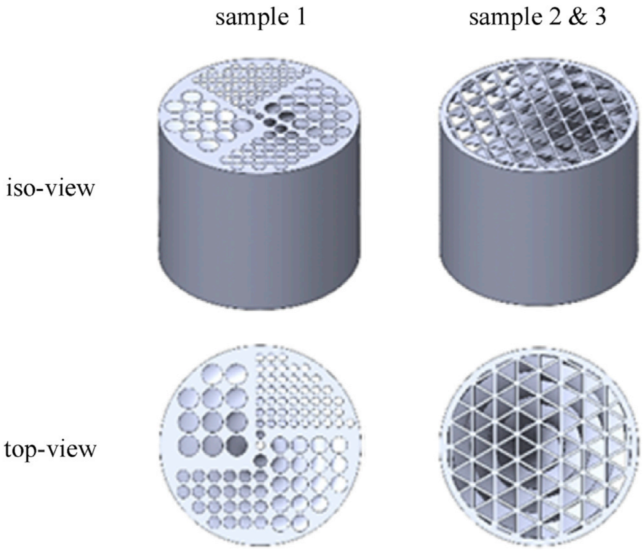

Fig. 8. Iso- and top-view of the tested samples.

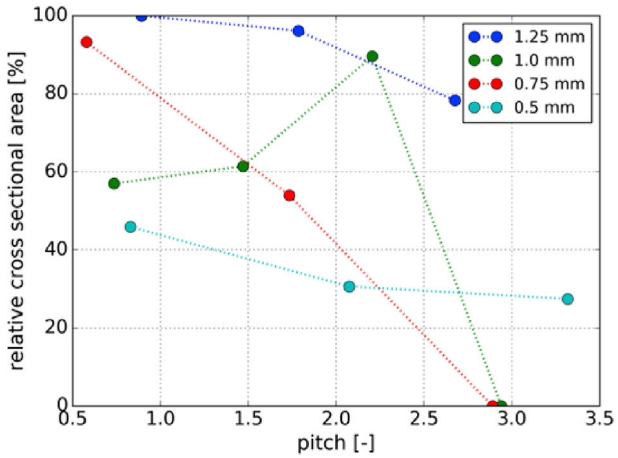

Fig. 9. Relative cross sectional area at 4.43 mm.

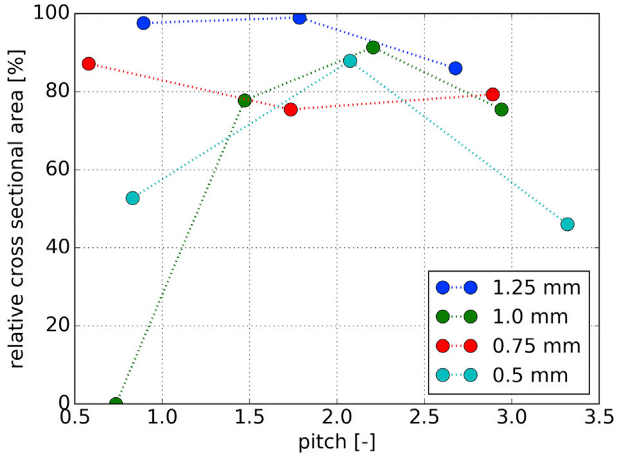

Fig. 10. Relative cross sectional area at 9.11 mm.

The results for sample 2 and 3 are shown in Fig. 11. The circular symbols refer to sample 2 and the triangles to sample 3. The plot shows that even for a small pitch, the cross section area is just above 80%. This can partly be explained by the manufacturing process. Due to glare parts

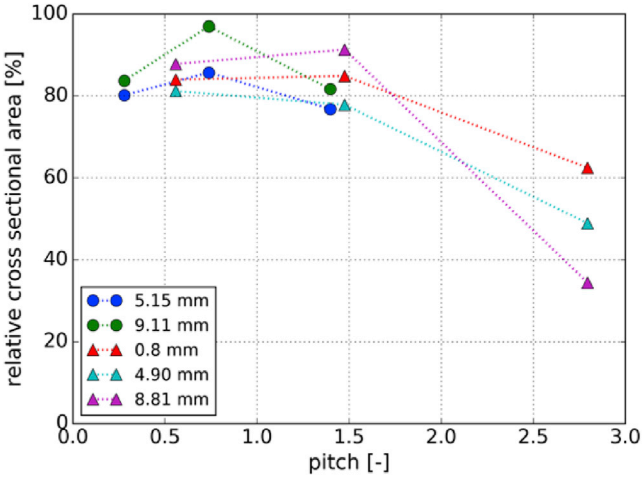

Fig. 11. Relative cross section area for triangular channels.

of the liquid suspension is irradiated that is not supposed to be cured. This effect is especially noticeable at sharp corners. The subsequent dissolving of excess slurry from these corners is also hindered by effective diffusion effects. The overall result is a smaller cross sectional area. For a pitch of up to about 1.5 the results are independent of the pitch. A pitch larger than 2.5 clearly affects the result, which was already concluded from Figs. 9 and 10.

Note that the here presented structure where used to identify manufacturing limitations only. The next step in development of such monoliths will be to investigate how the inner structure can be optimised such that a homogeneous flow pattern in the monolith is obtained, resulting in the maximum amount of conversion for the least amount of pressure drop. A considerable amount of research will be spent on this within the RHEFORM project.

5.2.3. *Geometries of monolithic support*

Three different designs were chosen for the printed monoliths, as shown in Fig. 12. A classical design with straight channels was selected. It can also be manufactured by extrusion, thus it serves as a benchmark for the new designs and as a control group to evaluate the influence of the printing process itself. On the other hand, two designs based on 3D networks which can only be manufactured via ALM were selected.

One of the 3D designs called ‘cellular’ structure was taken due to considerations regarding maximising the macroporosity of the design. It is a classic lightweight design in the style of a gyroid and due to its large pore network, subsequent application of the washcoat is expected to be facilitated significantly.

The other 3D design was termed ‘polyhedral’ structure. The basic repetition unit in this case is a polyhedron with 26 faces. The basic idea with such a structure is the increase of the surface area inside the catalyst. In combination with the presence of turbulent flow behaviour inside the monolith, this design should lead to an increased performance.

5.2.4. *Monolithic supports: materials*

For the manufacturing of monoliths 4 different ceramic materials are being evaluated, cordierite ($(Mg,Fe)_2Al_4Si_5O_{18}$), aluminium oxide (Al_2O_3, alumina), magnesium oxide (MgO, magnesia) and silicon nitride (Si_3N_4). Their relevant (thermo)mechanical and electrical properties can be seen in Table 6.

All tested ceramic powders could be compounded into stable and photocurable ceramic suspensions that could be processed using Lithoz' LCM technology to print 3D parts (composites comprising the ceramic particles and a photopolymer network acting as a temporary scaffold). Upon exposure to elevated temperatures the photopolymer was burned off and the ceramic particles were sintered together to give the final ceramic parts.

Table 6
(Thermo)mechanical and electrical properties of evaluated ceramic materials, based on [22].

Properties	Alumina >99% Al_2O_3	Cordierite	Magnesia dense	Silicon nitride
Open porosity [vol%]	0	0.5	0	0
Density [g/cm^3]	3.7	2.1	3.4	3.2–3.3
Young's modulus [GPa]	300	n/a	250	290–330
Mean coeff of therm exp at 30–1000 °C [10^{-6} K^{-1}]	7–8	2–4	13.5	2.5–3.5
Specific heat capacity at 30–1000° C [J kg^{-1} K^{-1}]	850–1050	800–1200	850–1050	700–850
Thermal conductivity at 30–100° C [W/m K]	19–30	1–2.5	7–11	15–40
Max. Operating Temperature [° C]	1400–1700	1200	800–2000	1300
Thermal shock resistance [rated]	good	very good	good	good

5.2.5. *Monolithic catalyst: washcoating*

The monoliths display only macroporosity and the surface area is low. Therefore, it is important to increase the surface area before the impregnation by adding a porous layer to the external surface of the monolith that is the geometric surface of the walls of the channels.

Procedures were developed based on colloidal solutions of aluminium, alumina and or aluminium oxohydroxide named sol AU and sol DUS. The parameters that have to be carefully controlled are the temperature, the viscosity of the washcoating suspension (depending of the size and the tortuosity of the channels), the duration of the procedure, and the drying conditions. 3D-printed specimens are dipped into the sols selected. They are then gently blown, dried at room temperature and calcined in a muffle furnace.

5.2.6. *Monolithic catalyst: active phase*

The active phase was deposited only once the washcoating of the different monolithic materials was shown as feasible. The deposition of the active phase is carried out by impregnating the washcoated monoliths with a solution of the active phase precursor at room temperature. The solvent is then removed by gentle evaporation at moderate temperature. The activation procedure is a critical step and depends on the nature of the active phase. The activation is conducted at higher temperatures, under oxygen and/or hydrogen, depending on the nature of the targeted active phase.

5.3. *Catalysts testing in batch reactor*

5.3.1. *Batch reactor setup*

A preliminary catalyst selection was conducted with a batch reactor. This lab-scale homemade setup has been fabricated to acquire pressure and temperature data during the catalytic reaction of different monopropellant-catalyst pairs [23]. Fig. 13 shows photographs and a scheme of the setup. The reactor is a constant volume batch reactor (172.5 mL, stainless steel AISI-316L) with operating pressure between 0.01 mbar and 2 bar.

Three thermocouples (TR) are placed in the heating elements, inside the catalyst bed, and in the atmosphere of the reactor respectively. One

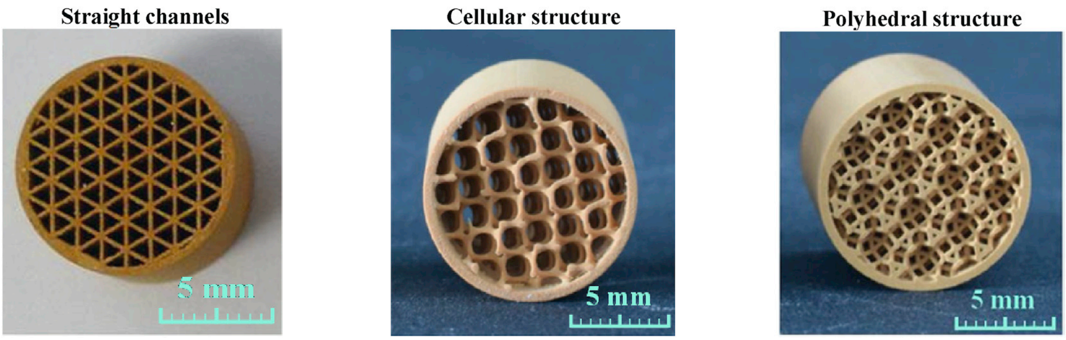

Fig. 12. Designs of monolithic supports.

Fig. 13. Photographs and scheme of the batch reactor.

gauge (PR) measures the pressure in the reactor. The sensors are connected to the computer through a Netdaq 2645A interface (Fluke Company, Canada). Acquisition is computed via a LabView virtual instrument developed in the lab at 5 Hz.

The catalyst can be preheated in the 20–350 °C range and two operation modes are achieved: constant temperature mode and temperature increase mode. The catalyst is placed inside a dedicated sample pan comprising a conical flange to prevent the loss of sample after possible ejections during the exothermic decomposition, see scheme in Fig. 13. The monopropellant is added using a microsyringe (Hamilton 100 μL) through a septum.

All tests were done on granules with grain size ranging from 100 to 250 μm. The reactor was purged under argon at 60 mL min^{-1} for 1 h (*ca.* twenty times the volume of the reactor) prior to propellant injection. The heating rate was set to 10 °C min^{-1}. Fig. 14 shows the temperature and pressure profiles typically obtained. Based on these profiles several parameters are identified:

- Decomposition temperature (T_{dec}). A sudden increase in temperature and pressure is measured at this temperature due to the energy release associated to the decomposition of the propellant.
- Maximum measured temperature (T_{max})
- Temperature increase ($\Delta T = T_{\mathrm{max}}$ - T_{dec})
- Maximum pressure (P_{max})

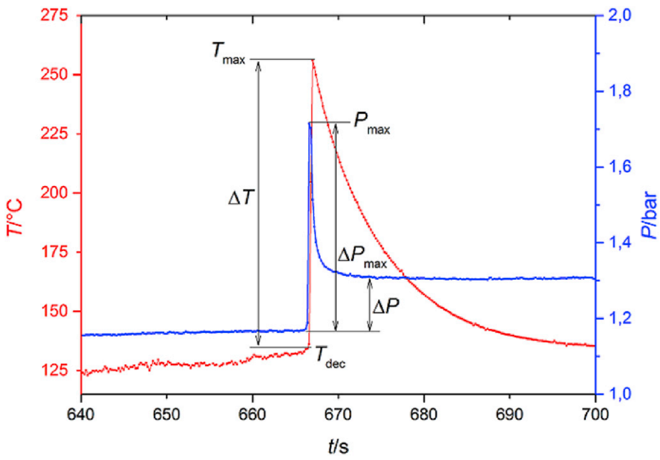

Fig. 14. Temperature and pressure *vs.* time defining the profile parameters during propellant catalytic decomposition.

- Pressure increase (ΔP_{max}) between the initial condition and the maximum pressure
- Pressure increase (ΔP) between the initial condition and the steady-state pressure after decomposition
- Temperature increase rate (s_p) represents the temperature rate between T_{dec} and T_{max} so that it corresponds to the slope the temperature rising.

5.3.2. *Batch reactor: results*

The preliminary decomposition test data obtained from the batch reactor results are gathered in Table 7. Both baseline monopropellants have been used and the decomposition has been performed on granulated catalysts.

Catalysts behaviour seems to be correlated to the specific surface area of the support material. DUS1 exhibits the highest one (Table 5) and leads to the lowest T_{dec}. The tested active phase acted differently on FLP-106 and LMP-103S. As an example, for FLP-106, the catalyst based on DUS1 calcined at 1200 °C is able to initiate the decomposition of the propellant at 104 °C while LMP-103S ignites at a higher temperature of 115 °C with the same catalyst.

From preliminary tests conducted, promising results have been obtained. Catalytic decomposition allows a decrease of the T_{dec} of about 44 °C for FLP-106 and 19 °C for LMP-103S in the presence of DUS1-based catalyst calcined at 1200 °C. The pressure increase (*Sp*) was improved with almost all the catalysts tested for both propellants compared to the thermal ignition. An increase of the ΔP_{max} and/or the ΔP value is also observed.

The search for the optimal nature and percentage of active phases is still ongoing.

6. Development of thermal igniters

6.1. *Resistive ignition*

Two advanced thermal ignition methods, resistive and laser, were tested with ADN-based propellants [24].

In the tests conducted on resistive ignition, a current was discharged through a drop of propellant. ADN based propellants are ionic solutions and therefore good electric conductors. When a current flows through the propellant, the propellant will heat up due to its inherent resistance.

The test rig, shown in Fig. 15, has interchangeable electrodes. The gap distance can be regulated. Initially a flat lower electrode and a slightly curved upper electrode were used. The curvature of the electrode keeps the drop in the centre of the gap. A pointy upper electrode was later used,

Table 7

Batch reactor decomposition test results conducted on LMP-103S and FLP-106 in the presence of selected powdered catalysts. (*) heat treatment temperature of the catalysts in air before test.

Nature of the support	Active phase	Propellant	T_{dec} [°C]	T_{max} [°C]	ΔT [°C]	s_T [°C/s]	ΔP_{max} [bar]	ΔP [bar]	s_P [bar/s]
"Thermal"	–	LMP-103S	134	281	147	53	0.15	0.06	0.07
		FLP-106	148	330	182	91	0.24	0.03	0.24
DUS 1	Pt—Cu	LMP-103S	115	219	104	260	0.40	0.06	2.00
(1200 °C)*		FLP-106	104	192	88	88	0.37	0.09	0.37
Hexa B	Pt—Cu	LMP-103S	146	206	60	300	0.46	0.06	2.32
(1500 °C)*		FLP-106	124	210	89	61	0.25	0.08	0.41

in combination with a bowl shaped lower electrode. All tests were made at ambient pressure.

The tests were filmed with a Photron SA5 fast cam. The frame rate was varied from 50 fps to 10000 fps but most tests were filmed at 1000 fps.

The voltage was generated by a high voltage supply. Three 1000 μF capacitors in series were used, each with a maximum voltage rating of 500 V. The effective capacity was 1000/3 μF and the effective maximum voltage 1500 V. A BitScope Micro oscilloscope controlled by a Raspberry Pi 1 B + were used in the measurements. The BitScope has two analogue channels and eight digital channels. The analogue signal input channel was used for the data acquisition and one digital input channel for triggering. The current was measured with a Pearson probe with an output of 0.001 (V/A). The Raspberry Pi 1B+ controlled the supply voltage with a 12 bit DAC. An insulated-gate bipolar transistor (IGBT) was used to release the electric current. A button was used as a switch. The wiring limited the maximum voltage to 500 V.

Around 150 tests were conducted changing several test parameters. Initially the amount of propellant used was 10 μL. After a few tests, it was decided to reduce the volume to 2 μL. This is the smallest amount of propellant which created a drop that could be seen clearly when filming. The voltage was varied between 60 V and 350 V, in order to find the optimum voltage for resistive heating. The discharge current was observed and recorded. A large current was measured when a spark was generated. In the other tests, in which no arc discharge occurred, a discharge rate smaller than the one calculated based on propellants conductivities was measured. This indicates larger impedances of the propellants together with electrode surfaces.

The high speed video indicated no ignition in any of the tests conducted, but an interesting effect happening during the current flow phase could be observed between the two electrodes. The drop loses contact with the upper electrode and later regains the contact with this electrode. When the voltage was increased to 200 V or higher, the drop is splashed away by the current, as shown in Fig. 16. Tests were conducted with different electrode gap heights. During the tests it was observed that the drop loses contact with the upper electrodes during the first phase of discharge. The use of wider gaps seems not to be suitable for ignition, due to the fact that with larger gaps the drop does not regain contact with the upper electrode due to gravitational effects. On the other hand, when the gap was smaller than 0.3 mm it was possible to obtain some sparks, probably due to electrical arcs. However, they did not have enough energy to ignite the propellant. Electric arcs are not desired since they do not contribute to resistive heating. The goal was to verify resistive ignition of the propellants, and not ignition through arc discharge.

Two different geometries of electrodes were tested. Initially the tests were conducted with flat electrodes. Subsequently, in order to avoid splashing, a bowl shaped lower electrode was designed. Also with this shape it was not possible to ignite the propellant.

Tests were conducted with both FLP-106 and LMP-103S. As previously mentioned, during some tests sparks generation occurred. In order to verify if the sparks were generated by an electric arc or by an interaction of the electric current with the propellant, tests were repeated using an aqueous solution of NaCl instead of propellants. Such solution is non-ignitable. The results obtained using the same test configuration and with the 3 different test fluids did not show apparent difference in the sparks formed.

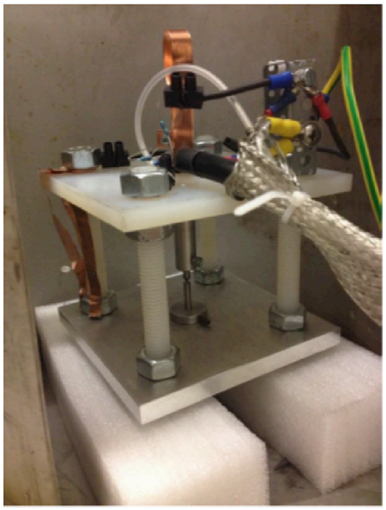

Fig. 15. Resistive heating experimental setup.

Initially the tests were conducted with mild steel electrodes. Then the electrodes were changed to tungsten. The result of this was the same as previous tests but without any spark formation. Optically it was observed that changes of the propellant under influence of electric current took place. Bubbles were formed and the colour became more yellowish. Bubbling might be the reason for interfering with the resistive heating. If a significant fraction of the droplet is bubbles this will change its resistance. Some vapour was detected during the tests and it seems that only the liquid ingredients vaporized. In the case of FLP-106, water has much lower boiling temperature than the two other ingredients ADN and monomethylformamide (MMF). In a slow heating probably the water boils off. That could explain the propellant changing to a more yellow colour. The liquid ingredients of LMP-103S, methanol and an aqueous solution of ammonia, are quite volatile. In several tests all liquid compounds in LMP-103 vaporized.

The results show that it is hard to obtain ignition by using resistive heating. In the setup used no ignition was obtained.

6.2. *Laser ignition*

The experimental setup used for the laser ignition tests is shown in Fig. 17. The main components of the experimental setup were: an acoustic levitator, a Nd:YAG pulsed laser, a high speed camera, and a LED backlighting.

An ultrasonic acoustic levitator from the company tec5 was used. It operated with an acoustic frequency of 58 kHz. A pulsed, high-energy Nd:YAG laser YG980 from Quantel was used. For the carried-out tests in the present work the fundamental laser wavelength of 1064 nm was chosen. High speed shadowgraph images were recorded with a Photron SA1.1 high speed camera, with an acquisition rate of 300 000 fps and a resolution of 128 × 64 pixels. The background lighting was provided by a LED light source.

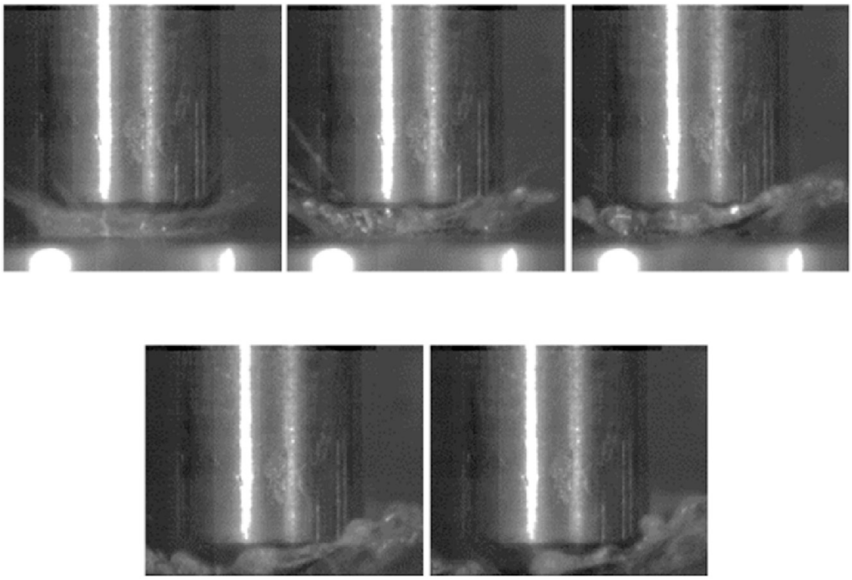

Fig. 16. Series of splashing propellant. From time (in ms) 0 to 4 in 1 ms increments.

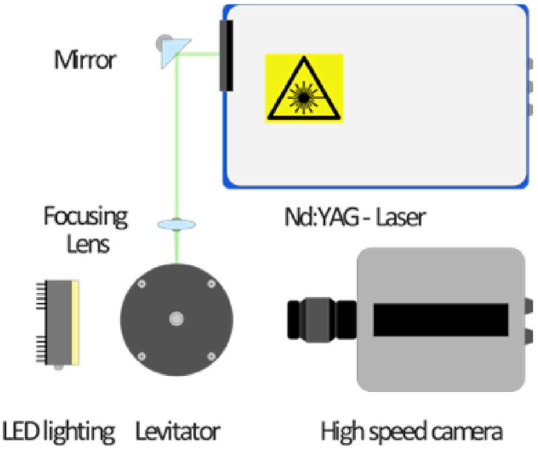

Fig. 17. Schematic drawing of the experimental setup.

The tests were conducted suspending a droplet of propellant the levitator. The laser was focused to generate a plasma in the proximity of the droplet. Laser ignition tests were conducted with the baseline propellants as well as with variations of these propellants with increased water content, with the composition listed in Table 2.

The energy of the laser pulse was high enough to generate a spark in ambient air. The spark is caused by the formation of a high-temperature plasma from the breakdown of the air molecules excited by the laser. The formation of the plasma generates a blast wave that leads to an aerodynamic deformation of the droplets, as explained in [25]. A strong emission of light from the drop followed the laser pulse. An example of the shadowgraph images obtained is shown in Fig. 18. An analysis was conducted counting the number of frames with luminous emission after the laser pulse. The time length in which the droplet remained bright varied from few μs up to 100 μs. No clear trend was recognized. Similarly, results scattered when repeating the tests with the same propellants under equal conditions.

The diagnostic technique used during the tests (high speed shadowgraphy) did not allow determining the causes of light emission. Light is for sure generated by the plasma emission due to the laser induced breakdown. The duration of the plasma emission in air is few microseconds (10–20 μs). Another source of light could be combustion or the decomposition of the propellants. Another effect could be reflections of light inside the drop.

6.3. *Torch igniter*

In the RHEFORM project there was not sufficient time to try to improve resistive and laser ignition methods. A proven hydrogen/oxygen torch igniter has been therefore selected for the subsequent thermal ignition tests. It is extremely flexible: by changing the amount of

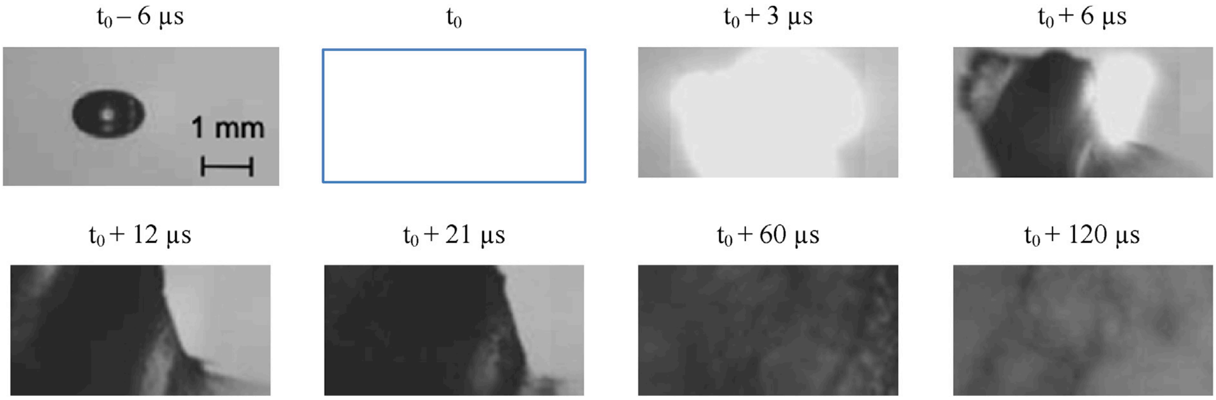

Fig. 18. Shadowgraph images obtained during laser test. Propellant: LMP-103S + 5.8% Water.

hydrogen and oxygen it is possible to change the amount of power delivered as well as the temperature of the combustion gases generated. A torch igniter can deliver a considerable amount of thermal power: the model used for the ignition tests in the present work could deliver up to 20 kW. It allows a large number of restarts, which is particularly interesting while testing.

A thermal ignition demonstrator based on a torch igniter has been designed and manufactured, and is shown in Fig. 19. The pressure sensors used were Kistler 4045 (Full scale: 50 bar), except the one mounted on torch igniter, which was a Measurement sensor (Full scale: 50 bar). Thermocouples type K, from Elektronic Sensor were used. Two pressure sensors were mounted in the combustion chamber. Pressure sensors and thermocouples were positioned in the feeding line just after the tank and before the injector. Pressure and temperature sensors were mounted in the oxygen and hydrogen feeding lines, before the sonic orifices, allowing the determination of the mass flow rates of the two gasses. The propellant flow rate was measured with a turbine from PMT, with a measuring range of 33 mL/s to 470 mL/s.

In all the tests the torch had an oxidizer to fuel mixture ratio (ROF) of around 1.5 and a power of 16 kW. The demonstrator was tested initially with FLP-106. 13 tests were conducted in total:

- 8 Tests with torch igniter, 8 mm exit nozzle, swirl injector type 3 (the largest of the swirl injectors considered), with different mass flow rates (from around 100 g/s to below 50 g/s) and different overlapping time between torch and propellant injection. The propellant vaporized as long as the torch was on. No ignition was observed.
- 2 Tests with same configuration as above but without nozzle. Tank pressures 3.8 and 2.6 bar, flow rate below 30 mL/s and therefore not measurable with the turbine used. The propellant vaporizes in the chamber. Combustion outside the chamber was observed, probably with the use of atmospheric oxygen.
- 2 Tests with torch igniter and chamber pre-heating through an electrical heating band. 8 mm exit nozzle. Smaller swirl injector type 2. Mass flow rates: 50 and 40 g/s. In the test conducted with the lower mass flow rate several pressure peaks were measured in the combustion chamber, probably due to local ignition.
- 2 Tests with same configuration as above but without nozzle. Tank pressures 3.8 and 2.0 bar, flow rate not measurable. In the test with the lower pressure the flame was brighter, probably due to ignition.
- 1 Test with only band and without nozzle. Tank pressure 2.0 bar. The band did not have enough power to completely vaporize the propellant. No ignition was observed.

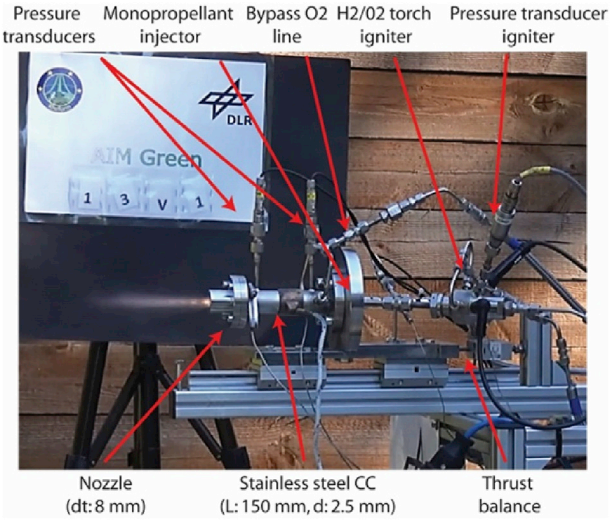

Fig. 19. Thermal ignition demonstrator.

5 tests were conducted with LMP-103S:

- 4 Tests with torch igniter, 8 mm exit nozzle, swirl injector type 1 (smaller than the other one used for FLP-106). The first three tests were aborted due to a red line generated by a priming effect in the feeding line. The tank pressure in the fourth test was reduced, in order to reduce the pressure overshot. In this test the torch vaporized the propellant, but no ignition was observed.
- 1 Test with torch igniter, 8 mm exit nozzle, swirl injector type 1, and additional oxygen injected directly in the chamber. The mass flow rate of oxygen was selected in order to achieve a ROF of around 6 in the chamber. In this test the propellant, or probable only some components of the propellant reacted. The pressure in the combustion chamber oscillated, with an average value of around 8 bar. The combustion stopped as soon as the additional oxygen was shut off.

The ignitor demonstrator was severely damaged from a detonation which took place after the shut-down. The cause was probably the vaporization of the liquid components contained in the propellant (water, methanol and ammonia) leaving as residual pure ADN on the combustion chamber wall and in the feeding lines. Pure ADN is an explosive and detonated probably due to contact with a hot spot. The tests conducted proved that the torch igniter in the configurations tested is unsuitable to ignite the two baseline propellants, FLP-106 and LMP-103S. Through the tests, a better understanding of the thermal ignition of ADN-based monopropellants and their reaction behaviour was acquired. The working hypothesis is that the decomposition of the propellant requires some kind of reaction holding device in the chamber. A demonstrator is currently designed and manufactured in order to verify this hypothesis.

7. Conclusions

RHEFORM is a European project focused on the replacement of hydrazine in orbital and launcher applications. The present work describes the results obtained in the first half of the project. Goal of RHEFORM is to develop new technologies to overcome some of the limitations of monopropellants based on ammonium dinitramide (ADN). Two reference thrust classes have been considered: 20 N and 200 N. LMP-103S and FLP-106 have been selected as baseline propellants. Variations of the baseline propellants with increased water content have been studied. The amounts of water necessary to obtain combustion temperatures compatible with several potential chamber construction materials have been determined. The propellant variations were characterized using vibrational spectroscopic techniques. The solubility of ADN in different solvents was measured at two different temperatures, -5 and -10 °C.

New catalysts are being developed. Two types of catalyst supports are investigated: granulated and monolithic. A model has been implemented to describe how the void fraction distribution is influenced by the bed wall as function of the shape and size of the granules. Monolithic supports are manufactured with an innovative 3D printing technique called Lithography-based Ceramic Manufacturing (LCM). In order to investigate manufacturing limitations, complex monolithic structures have been produced. These monoliths were different to different cross sections and the size of the channels was measured and compared.

Preliminary ignition tests were conducted using a laser and a resistive igniter. The propellants proved difficult to ignite, probably due to the high water content. Subsequently the works on thermal igniter focused on a H_2/O_2 torch igniter. The tests conducted proved that the torch igniter in the configurations tested is unsuitable to ignite the two baseline propellants, FLP-106 and LMP-103S. Through the tests, a better understanding of the thermal ignition of ADN-based monopropellants was acquired. The working hypothesis is that the decomposition of the propellant requires some kind of reaction holding device in the chamber.

Acknowledgments

This project has received funding from the European Union's Horizon 2020 research and innovation programme under grant agreement No 640376.

References

[1] Rheform - Project Website," [Online]. Available: www.rheform-h2020.eu. [Accessed 17 05 2017].

[2] C.D. Brown, Spacecraft Propulsion, AIAA Education Series, Washington, DC, 1995.

[3] European Chemicals Agency (ECHA), Hydrazine - substance information [Online]. Available: https://echa.europa.eu/substance-information/-/substanceinfo/100.005.560. (Accessed 17 May 2017).

[4] A.S. Gohardani, J. Stanojev, A. Demairé, K. Anflo, M. Persson, N. Wingborg, C. Nilsson, Green space propulsion: opportunities and prospects, Prog. Aerosp. Sci. 71 (2014) 128–149.

[5] K. Anflo, B. Crowe, In-space demonstration of an ADN-based propulsion system, in: 47th AIAA/ASME/SAE/ASEE Joint Propulsion Conference & Exhibit, AIAA, San Diego, California, 2011, 2011-5832.

[6] A.S. Kesten, Analytical Study of Catalytic Reactors for Hydrazine Decomposition, United Aircraft Research Laboratories, East Hartford, Connecticut, USA, 1968.

[7] A. Iffly, A. Jamin, L. Lecardonnel, An EcosimPro Model of Herschel and Planck Propulsion Systems, Space Propulsion, San Sebastian, Spain, 2010.

[8] Airbus Safran Launchers, "VEGA Small Launcher," [Online]. Available: http://www.space-propulsion.com/spacecraft-propulsion/showcase/vega-small-launcher.html. [Accessed 17 05 2017].

[9] S. Gordon, B. McBride, Computer Program for Calculation of Complex Chemical Equilibrium Compositions and Applications, NASA RP-1311, 1994.

[10] M. Negri, Replacement of hydrazine: overview and first results of the H2020 project Rheform, in: 6th European Conference for Aeronautics and Space Sciences (EUCASS), 2015. Krakow, PL.

[11] M. Wurdak, F. Strauss, L. Werling, H. Ciezki, D. Greuel, R. Lechler, N. Wingborg, D. Hasan, C. Scharlemann, Determination of fluid properties of the green propellant FLP-106 and related material and component testing with regard to applications in space missions, in: Space Propulsion Conference, 2012. Bordeaux, FR.

[12] A. Larsson, N. Wingborg, Green propellants based on ammonium dinitramide (ADN), in: Dr Jason Hall (Ed.), Advances in Spacecraft Technologie, InTech, 2011.

[13] N. Wingborg, A. Larsson, M. Elfsberg, P. Appelgren, Characterization and ignition of ADN-based liquid monopropellants, in: 41st AIAA/ASME/SAE/ASEE Joint Propulsion Conference & Exhibit, 2005. Tucson, Arizona.

[14] T.W. Price, D.D. Evans, The Status of Monopropellant Hydrazine Technology, Technical Report TR-32-1227, Jet Propulsion Laboratory, Pasadena, California, USA, 1968.

[15] R.E. Albers, Characterization of the performance of an industrial monolith reactor by accurate mapping of temperature differences, Catal. Today 105 (no. 3–4) (2005) 391–395.

[16] W. Zhang, Experimental and Computational Analysis of Random Cylinder Packings, Doctoral Dissertation, Louisiana State University and Agricultural & Mechanical College, Baton Rouge, LA, 2006.

[17] O. Bey, G. Eigenberger, Fluid flow through catalyst filled tubes, Chem. Eng. Sci. 52 (8) (1997) 1365–1376.

[18] R.B. Bird, W.E. Stewart, E.N. Lightfoot, Transport Phenomena, Rev. 2, New York: Wiley, 2007.

[19] S. Afandizadeh, E.A. Foumeny, Design of packed bed reactors: guides to catalyst shape, size, and loading selection, Appl. Therm. Eng. 21 (6) (2001) 669–682.

[20] M. Schwentenwein, J. Homa, Additive manufacturing of dense alumina ceramics, Int. J. Appl. Ceram. Technol. 12 (1) (2015) 1–7.

[21] A.D. Lantada, A. de Blas Romero, M. Schwentenwein, C. Jellinek, J. Homa, Lithography-based ceramic manufacture (LCM) of auxetic structures: present capabilities and challenges, Smart Mater. Struct. 25 (no. 5) (2016).

[22] Breviary Technical Ceramics, Association of the German Ceramics Industry, Lauf, Germany: Fahner Verlag, 2003.

[23] R. Eloirdi, S. Rossignol, C. Kappenstein, D. Duprez, N. Pillet, Monopropellant decomposition catalysts. III. Design and use of a batch reactor for catalytic decomposition of different monopropellants, J. Propuls. Power 19 (2003) (2003) 213–219.

[24] M. Negri, C. Hendrich, M. Wilhelm, D. Freudenmann, H.K. Ciezki, L. Gediminas, L. Adelöw, Thermal ignition of ADN-based propellants, in: Space Propulsion Conference, 2016. Rome, IT.